Journal of Applied Electrochemistry **30**: 347–357, 2000.

Effect of morphology on the performance of metal-hydride electrodes

K.M. SHAJU[1], V. GANESH KUMAR[1], S. RODRIGUES[1], N. MUNICHANDRAIAH[2] and A.K. SHUKLA[1]*
[1]*Solid State and Structural Chemistry Unit*
[2]*Department of Inorganic and Physical Chemistry, Indian Institute of Science, Bangalore-560012, India*
*(*author for correspondence, e-mail: shukla@sscu.iisc.ernet.in, fax: +91 80 3311310)*

Received 24 February 1999; accepted in revised form 31 August 1999

Key words: charge-transfer resistance, hydrogen-storage alloy, nickel/metal hydride cell, particle size effect

Abstract

Electrochemical studies on AB_2 type $Zr_{0.5}Ti_{0.5}V_{0.6}Cr_{0.2}Ni_{1.2}$ metal hydride electrodes with varying particle size suggests that the electrodes with alloy particles of about 60 μm yield the optimum performance. The values for diffusion coefficient of hydrogen in the alloy particles >25 μm are found to be nearly invariant. Both a.c. impedance and linear polarization data on electrodes with varying particle size suggest that the charge-transfer resistance depends on state-of-charge of the electrodes. A comparison of scanning electron micrographs of fresh electrodes and subsequent to their prolonged charge-discharge cycling suggests that the metal hydride particles develop stress-induced cracks owing to their inherent expansion and contraction during the hydriding/dehydriding processes.

1. Introduction

Nickel/metal hydride (Ni/MH) battery is now widely recognized as a substitute for the nickel/cadmium system for a variety of applications. The key factor in the development of the Ni/MH battery is the selection of an appropriate hydrogen-storage alloy to function as the negative electrode [1–3]. Various alloys that have been employed as negative electrode material in Ni/MH cells belonging to the AB_2 and AB_5 series. Among these, zirconium-based AB_2 alloys are documented as the most appropriate metal hydride electrode materials [4–6]. The composition and preparatory conditions of electrodes have been reported to affect their performance [7, 8].

The electrochemical hydrogen storage within the alloy during charging of the electrode in aqueous KOH electrolyte occurs according to the following reactions:

$$M + H_2O + e^- \rightarrow MH_{ad} + OH^- \quad (1)$$

Reaction 1 represents the formation of adsorbed hydrogen at the electrode/electrolyte interface through charge-transfer followed by absorption and subsequent diffusion of hydrogen into the bulk resulting in formation of the metal hydride depicted as

$$MH_{ad} \rightarrow MH_{ab} \quad (2)$$

$$MH_{ab} \rightarrow MH_{hyd} \quad (3)$$

where the subscripts ad, ab and hyd refer to adsorbed, absorbed and hydrided states, respectively. The reverse processes occur during discharge of the electrode. The performance of the metal hydride electrode is determined by the kinetics of Reaction 1 at the electrode/electrolyte interface, the rate of hydrogen diffusion within the bulk of the alloy and its specific hydrogen-storage capacity. The charge-transfer process controls the overall electrode reaction at low charge/discharge currents. At higher currents, the electrode reaction is, however, restrained by hydrogen diffusion within the bulk alloy. It is obvious that, if Reaction 1 determines the electrode capacity, a high active surface area is desirable. On the other hand, if diffusion of hydrogen in the alloy (i.e., Reaction 3) controls the electrode capacity, an optimization in particle size of the constituent alloy powder would be desirable. However, an attempt to enhance the surface area of metal hydrides may lead to deleterious effects due to surface oxidation. In contrast, a higher particle size of the alloy may hinder hydrogen diffusion within the bulk alloy and hence a reduction in charge storage. Therefore, it is mandatory to optimize the particle size and morphology of the alloy constituting the metal hydride electrode for improved performance.

In the literature [9–11], there are a few reports on the influence of surface modification of metal hydrides and the electrode performance. For example, ball milling of Mg_2Ni alloy brings about a reduction in its particle size with a positive effect on its charge storage [9]. By contrast, for $ZrCr_{0.4}Mn_{0.2}V_{0.1}Ni_{1.3}$ alloy [10], continuous amorphization by ball milling substantially reduces its charge-storage capacity. Indeed, a recent study on a misch metal AB_5-alloy [11] shows that particle size has a

crucial role on the performance of metal hydride electrodes. In most cases, the change in capacities is ascribed to the collapse in crystal structure and/or due to a change in the surface activity of the alloy. Since the effect of surface modification on electrode performance differs from system to system, it is imperative to examine it for different alloys.

In the literature [12–18], both impedance spectroscopy and linear polarization techniques have been employed to study the kinetics of charge–discharge and diffusion processes during the hydrogen absorption/desorption reactions. The electrode kinetic parameters obtained from a.c. impedance studies have been found to compliment the linear polarization studies. In this communication we report systematic morphological and electrochemical studies employing both impedance and linear polarization measurements to identify the kinetic parameters for metal hydride electrodes with varying particle size of the $Zr_{0.5}Ti_{0.5}V_{0.6}Cr_{0.2}Ni_{1.2}$ alloy.

2. Experimental details

2.1. *Alloy preparation and physicochemical characterization*

Ingots of $Zr_{0.5}Ti_{0.5}V_{0.6}Cr_{0.2}Ni_{1.2}$ alloy each weighing about 600 g, were obtained by arc melting of spongy constituent elements under argon atmosphere at 10^{-3} to 10^{-4} Pa in water-cooled copper crucibles. Morphological and compositional analyses of the alloy were carried out on a Jeol-JSM-840A scanning electron microscope coupled with an Oxford-ISIS elemental analyser. After mechanical pulverization, the ingot was separated into various particle sizes by passing it through graded sieves, namely 97–146 μm (100–150 mesh), 86–97 μm (150–170 mesh), 73–86 μm (170–200 mesh), 49–73 μm (200–300 mesh), 42–49 μm (300–350 mesh), and <42 μm (350 mesh). The average of the extreme sizes from each batch was taken for data presentation and discussion. Particle-size analyses for various ranges of alloy particles were also carried out on a Malvern (UK) Mastersizer-X ver. 1.2 by using the polydisperse model. The X-ray powder diffraction (XRD) patterns of powders with different particle size were recorded on a Siemens-D 5005 X-ray diffractometer using CuK_α radiation.

2.2. *Electrochemical studies*

Roll-compacted negative electrodes were prepared from powders with varying particle size. The dough obtained by mixing the alloy powder (85 wt %), graphite (10 wt %), and polytetrafluoroethylene (PTFE)-GP2 Fluon suspension (5 wt %) was rolled into a thin sheet and folded around a degreased nickel mesh (24 mm × 30 mm); the loading of active material on each electrode was 800 mg. The details of electrode fabrication have been reported elsewhere [4]. The electrochemical cell for the electrode characterization was assembled with metal hydride negative electrode, nickel-positive electrode, and a Hg/HgO, OH^- (6 M KOH) reference electrode (MMO). All the potentials were measured with respect to the MMO reference electrode. The state-of-charge (SOC) value of the metal hydride electrode was taken as zero when the potential was −600 mV vs MMO.

To monitor the potentiodynamic behaviour of the bulk alloy, the ingots were sliced to obtain alloy pieces of dimensions: 20 mm × 20 mm × 2 mm. These alloy pieces were mounted on a spring loaded Teflon sample holder with stainless steel connectors. The electrochemical cell for the characterization of the ingot metal hydride electrode was assembled akin to that for the roll-compacted electrodes, with the ingot slice as the negative electrode.

The linear sweep voltammograms of the electrodes were obtained at room temperature using an EG&G PARC Versastat driven by an IBM compatible computer and EG&G PARC model M-270 electrochemical software. The equilibrium potential (E_e) and exchange current density for electrodes with different particle sizes was determined as a function of the SOC values. Impedance measurements on the metal hydride electrodes at different SOC values were carried out using an EG&G PARC model-6310 electrochemical impedance analyser coupled to an IBM-PC and driven by EG&G model 398 software, in the frequency range 5 mHz–100 kHz with a signal amplitude of 5 mV. The impedance data were analysed by using a nonlinear least square (NLLS) fitting programe [19].

During the initial formation cycles, the electrodes were charged and discharged galvanostatically at $C/10$ rate. Subsequently, the electrodes were subjected to a charge–discharge schedule at $C/5$ rate. For a.c. impedance and d.c. polarization measurements, the electrodes were fully charged and kept at open-circuit stand for about 2 h to stabilize at open-circuit potential. For attaining different SOC values, the electrodes were discharged galvanostatically at $C/5$ rate for a predetermined period so as to attain the required SOC value. After discharging up to a required SOC value, the cell was kept at open -circuit stand for about 2 h to attain equilibrium conditions. The stable value of OCV (E_e) was noted and the linear-polarization experiments were carried out within ±15 mV around E_e at a scan rate of 1 mV s^{-1}. The cell was again left at open-circuit stand for 10 min prior to impedance measurements. This procedure was repeated for measurements at all SOC values.

3. Results and discussion

3.1. *Physicochemical characterization of the alloy*

The elemental composition of the alloy as obtained from energy dispersive analysis of X-rays (EDAX) by aver-

aging the results from ten randomly chosen spots was found to be $Zr_{0.49}Ti_{0.46}V_{0.65}Cr_{0.21}Ni_{1.19}$. The particle size data for various ranges of sieved alloy powders were found to agree well within the ranges obtained from graded sieves. The typical data for particle size analysis of the 100–150 mesh size powder are shown in Figure 1. The sauter mean from the particle size analysis was found to be 124 μm, which is in close agreement with the average value of the sieve range, namely 122 μm. The X-ray diffraction (XRD) patterns obtained for the powders with three different particle sizes are shown in Figure 2. It is clear from the XRD patterns that the powdering has little effect on the structure of the alloy particles.

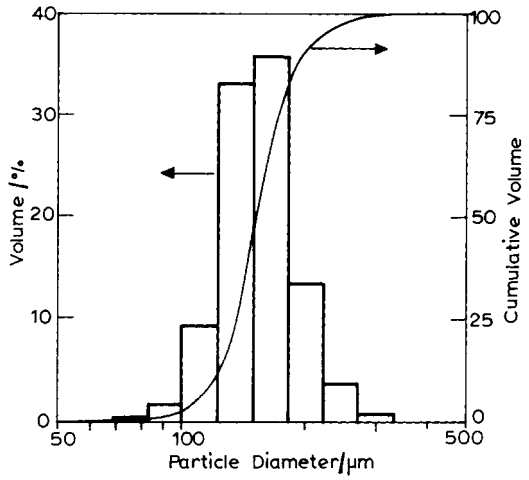

Fig. 1. Particle-size distribution for the 100–150 mesh size powders of the alloy.

3.2. *Electrochemical studies on the alloy ingot*

Potentiodynamic behavior of the alloy ingot was studied in 6 M KOH. On immersing the ingot electrode in the electrolyte, it showed an OCV of −0.3 V vs MMO. The voltammogram recorded in the potential region encompassing both the anodic and cathodic sides of OCV at a scan rate of 1 mV s^{-1} is shown in Figure 3. The voltammogram obtained on the freshly soaked ingot electrode (Figure 3, curve 1) shows an appreciably low current in the potential region negative to OCV and the current increases in the potential region of about −0.95 V vs MMO due to hydrogen evolution. In the potential region positive to OCV, the current increases from a low value, probably due to the oxidation of one of the metallic components of the alloy. Subsequent to the experiment, the OCV remained at about −0.3 V vs MMO thus suggesting that the hydrogen storage did not take place in the alloy sample during the potentiodynamic experiment. Therefore, a galvanostatic current of 10 mA cm^{-2} for about 1 h was passed through the electrode to enhance hydrogen evolution. Subsequent to the cessation of current, the electrode potential reached equilibrium OCV of about −0.9 V vs MMO, which is close to the theoretical value for the hydrogen evolution reaction. Thus, the ingot electrode behaved as a metal hydride electrode by absorption of hydrogen. The voltmmogram (Figure 3, curve 2) now showed higher magnitudes of current in both the cathodic and anodic potential regions. Hydrogen evolution and absorption into the electrodes occur in the cathodic regions. The current plateau between −0.9 and 0.15 V vs MMO is due to the oxidation of the absorbed hydrogen. At potentials beyond 0.15 V vs MMO, the increase in current is due to the oxidation of the ingot similar to curve 1. These data suggest that the present alloy can be safely used as a metal hydride electrode in the potential region up to about 0.15 V vs MMO without its oxidation.

3.3. *Electrochemical studies on roll-compacted electrodes*

The cycle-life data of the electrodes with different particle sizes are shown in Figure 4. During the initial

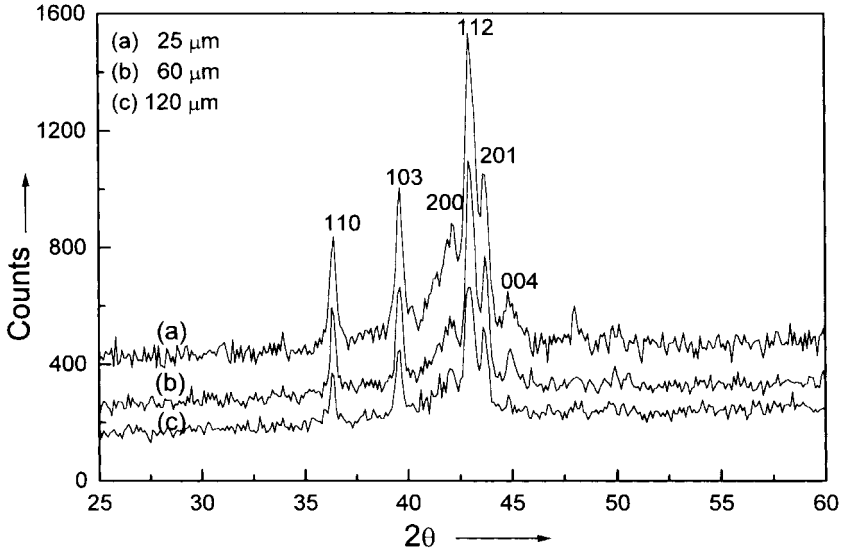

Fig. 2. Powder X-ray diffraction patterns for the alloy powders of particle size: (a) 25, (b) 60 and (c) 120 μm.

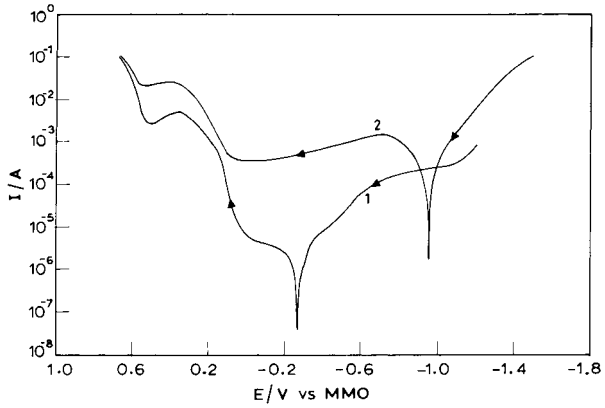

Fig. 3. Cyclic voltamogram of the alloy ingot (4 cm^2) at scan rate of 1 mV s^{-1} before (1) and after (2) absorption of hydrogen.

cycles, the capacity is low for all the electrodes. But, subsequent to about the seventh charge-discharge cycle, the electrodes yield nearly stable capacity values except for the electrode with alloy particles of ~25 μm. The capacity of the electrodes with particles of ~25 μm is not stable even after their formation and shows a continuous decrease with cycle number. The data on particle-size effect on discharge capacity of the electrodes obtained at different rates of discharge at room temperature are shown in Figure 5. It is evident that, at lower rates of discharge, the electrodes with higher particle size (average particle size 120 μm) are superior in performance with a maximum specific capacity of 320 mA h g^{-1}. By contrast, at higher discharge rates, the capacity values for the electrodes decrease monotonically with increasing particle size except for the electrodes with particles of ~25 μm which yield lowest discharge capacity at all rates.

The grain size, surface morphology of the alloy particles, charge-transfer kinetics at the electrode/electrolyte interface, and diffusion of hydrogen in the alloy normally determine the dischargeability of the alloy. The lower capacity values observed for electrodes with particles of ~25 μm may be due to a partial surface oxidation of the alloy and/or due to the lower porosity of the electrodes, both of which suppress the effective surface-area for hydrogen adsorption. The observation that the electrodes with higher particles are superior in performance at lower rates of discharge suggests that the lower-sized particles have more inactive surface and diffusion does not limit the discharge process at lower rates. Furthermore, the higher discharge capacity values observed for electrodes with higher particle sizes at lower discharge currents can be attributed to a more effective utilization of its charge-storage capacity. Since the electrode dischargability is mainly controlled by the charge-transfer reaction at the electrode/electrolyte interface, a higher active-electrode surface area would yield a higher discharge capacity. However, at higher rates of discharge, both the charge transfer at the interface and the diffusion of hydrogen in the bulk alloy would determine the discharge capacity. The low capacity values observed at high discharge rates for electrodes with higher particle size may mainly be due to the restricted diffusion of hydrogen in the bulk alloy. The maximum capacity values at high discharge rates are obtained for metal hydride electrodes with particles ranging between 60–80 μm.

3.4. *Diffusion coefficient of hydrogen in the alloy powders*

Assuming constant flux at the surface and uniform initial concentration of hydrogen in the spherical alloy particles, the diffusion equation for large transition times (τ) is represented by [17, 18, 20, 21],

$$Q_r = Q^0 - \tau i = ia^2/15D \tag{4}$$

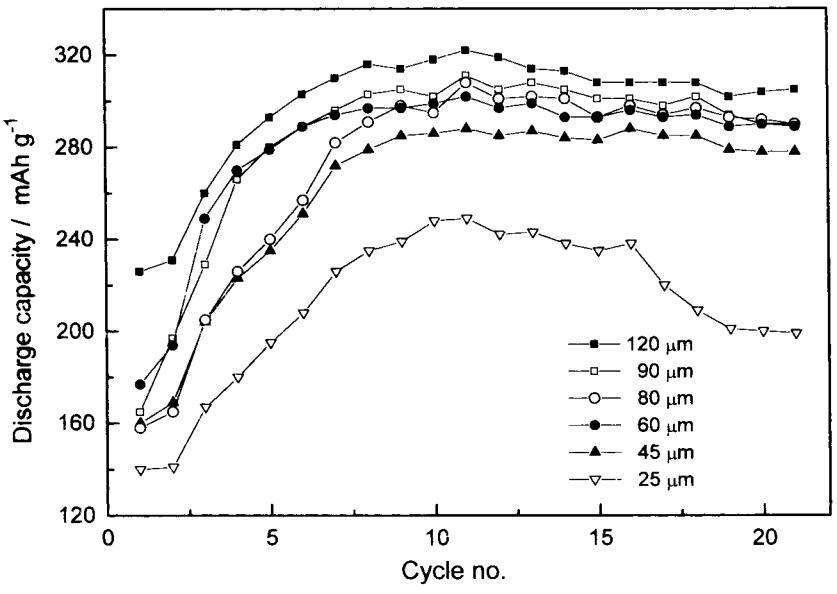

Fig. 4. Cycle life data obtained with charge/discharge current of 50 mA g^{-1} for the electrodes of different particle sizes.

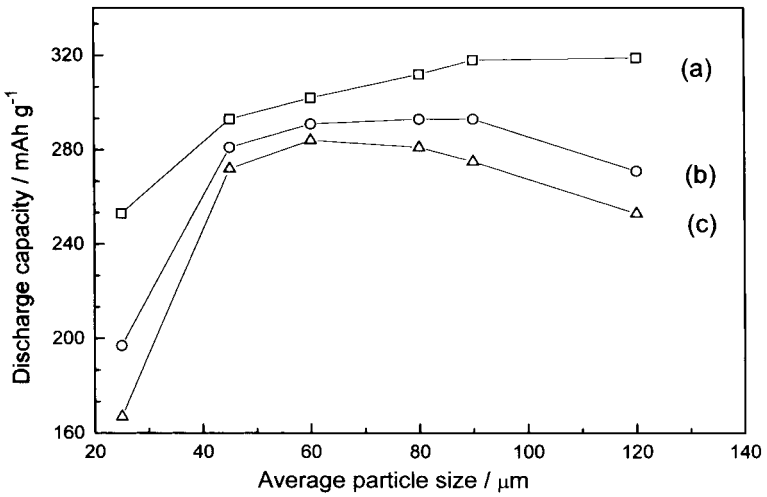

Fig. 5. Discharge capacities of formed electrodes with different particle size at various discharge current densities: (a) 50, (b) 80 and (c) 100 mA g^{-1}.

where Q_r and Q^0 are, respectively, the residual specific charge and initial specific charge (in C g^{-1}) in the alloy, i is the specific discharge current (in A g^{-1}), a is the average radius of the alloy particles and D is the diffusion coefficient of hydrogen in the alloy. The estimation of diffusion coefficient requires the values for residual capacity of the electrode (Q_r) after discharge up to the transient time (τ) and the mean particle size of the alloy. Since the same alloy composition was employed for different particle sizes, the theoretically attainable capacity per gram would be similar for all particle sizes. In practice, however, both the morphology and surface changes affect the hydrogen storage capacity of the alloys, as discussed earlier [9–11, 17]. In particular, surface oxidation of the alloy particles greatly reduces the amount of active material available for storage and hence hinders the electrode kinetics. Therefore, for the same alloy with varying particle sizes, the charge storage capacity differs appreciably. It is also found from the discharge capacity data at different rates that the hydrogen storage capacity is greater for alloys with higher particle size (Figure 6). Accordingly, the theoretical capacity value is not appropriate for calculating the diffusion coefficient. Hence, the intrinsic discharge capacity of the electrodes (for zero discharge current density) with different particle sizes have been estimated by extrapolating their discharge capacity versus discharge current plots to zero current [14]. The discharge capacities as a function of discharge rate for different particle sizes are shown in Figure 6(a). The discharge capacities of the electrodes of various particle size vary linearly with their discharge rates. Since the maximum attainable capacity is expected at zero rate of discharge, extrapolation of discharge capacity versus discharge rate plots to zero rate of discharge provides the maximum attainable capacity (Q^0). The Q^0 values thus obtained are also shown in Figure 6(b). It is found that the Q^0 value is greater for higher particle sizes. The theoretical capacity for the present alloy considering absorption of one hydrogen atom per metal atom is 440 mA h g^{-1}, which is not very different from its experimental value of 320 mA h g^{-1}.

For longer discharge schedules, the transient times can be obtained from the galvanostatic discharge curves as the time taken to discharge the electrode up to a cut-off voltage of −0.6 V vs MMO. The galvanostatic discharge curves for different rates of discharge for the electrodes with an average particle size of 60 μm are

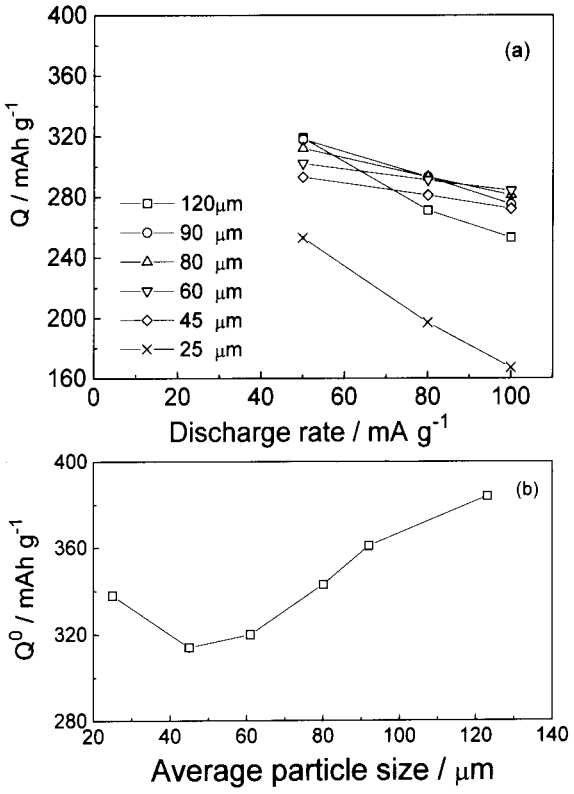

Fig. 6. (a) Discharge capacity (Q) as a function of discharge current density for electrodes with varying particle sizes and (b) maximum attainable capacity (Q^0) as a function of particle size.

shown in Figure 7(a) and for other particle sizes, namely, 25, 60 and 120 μm at $C/5$ rates in Figure 7(b). The observed transition times at different rates of discharge for electrodes with average particles of 60 μm were found to be 21.72, 12.9 and 10.8 ks, respectively, and the residual capacity (Q_r) of the respective electrodes after their discharge were found to be 64.8, 104.4, and 129.6 C g^{-1} for the discharge current densities of 50, 80, and 100 mA g^{-1}, respectively; the corresponding diffusion coefficients for hydrogen are 4.78×10^{-10}, 4.76×10^{-10} and 4.78×10^{-10} cm^2 s^{-1}. The values of diffusion coefficients for hydrogen (D) calculated for the alloys with different particle sizes are shown in Figure 7(c). These data show that the D value for alloy particles with an average particle size of 25 μm is $\sim 10^{-11}$ cm^2 s^{-1}; but is nearly invariant at $\sim 5 \times 10^{-10}$ cm^2 s^{-1} for alloy particles > 25 μm. It is noteworthy that the value of D obtained presently are higher than those reported for La-based hydrogen-storage alloys [13, 17] but are smaller to those obtained for Mm (misch metal)-based AB_5 alloys [22].

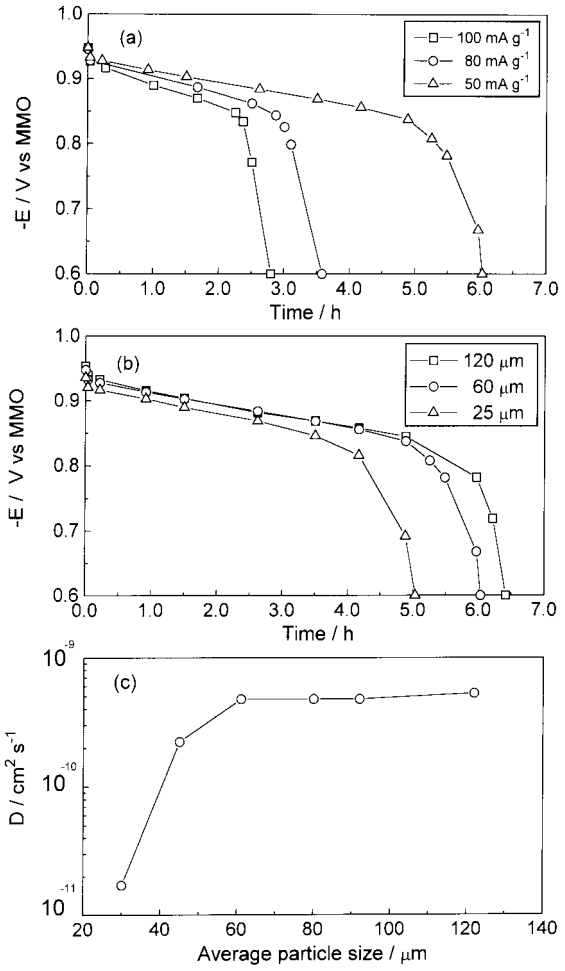

Fig. 7. (a) Galvanostatic discharge curves at different discharge current densities for electrodes of average particle size 60 μm, (b) discharge curves at a current density of 50 mA g^{-1} for electrodes of an average particle size 25, 60 and 120 μm, and (c) diffusion coefficient (D) as a function of particle size.

3.5. *Particle-size effect on impedance parameters and electrode kinetics of the electrodes*

The complex-impedance plots for the electrodes with different particle sizes subsequent to their formation are shown in Figure 8(a). Each spectrum consists of a pure resistive component (R_Ω) followed by two overlapped and depressed semicircles. This impedance behaviour can be modeled with an equivalent circuit shown in Figure 8(b). The resistive component (R_Ω) comprises the resistive contributions from the electrolyte, electrodes, current collectors, tags, terminals etc. The semicircles in the high frequency region were mainly attributed to be the resistive (R_1) and capacitive contributions arising from the electrode processing parameters [14, 23]. The impedance loci in the low frequency region represent the charge-transfer process (charge-transfer resistance R_{ct} and associated double-layer capacitance) at the electrode/electrolyte interface [6, 23]. The impedance parameters shown in Figure 8(b) were evaluated by using the NLLS fitting program [19]. The simulated impedance values derived from the equivalent circuit were found to fit well with the experimental data as shown in Figure 8(a). It is seen that, the electrodes exhibit a high R_{ct} prior to their formation. Subsequent to formation, R_{ct} decreases for electrodes of all alloy particle sizes. For the fully formed electrodes, R_{ct} shows an increase with decrease in alloy particle size as shown in Figure 8(a).

The linear-polarization data for electrodes with different particle sizes recorded at SOC values ~ 1 are shown in Figure 9. The values of R_{ct} were also evaluated from Figure 9 using Equation 5:

$$\left(\frac{d\eta}{di}\right)_{\eta=0} = R_{ct} = -\frac{RT}{F i_0} \tag{5}$$

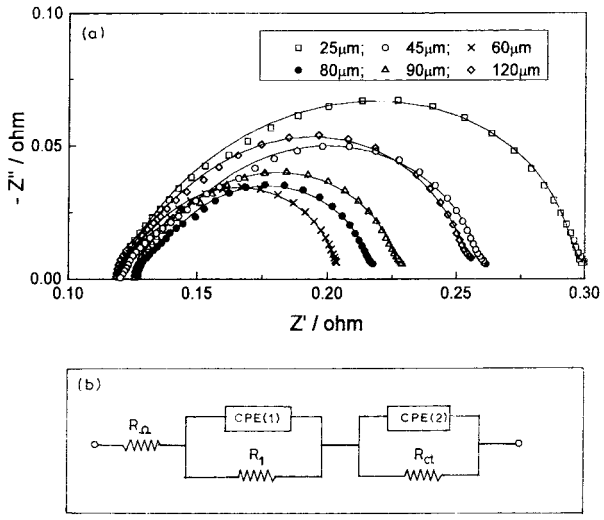

Fig. 8. (a) Complex impedance plots for electrodes with different particle sizes subsequent to their formation and (b) the equivalent circuit used for NLLS fit (alloy powder weight 0.8 g; electrode area 7.2 cm^2).

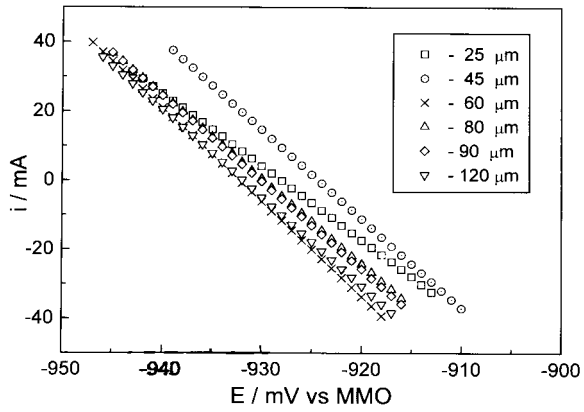

Fig. 9. Linear polarization data of the electrodes of different particle sizes obtained at a scan rate of 1 mV s^{-1} subsequent to their formation at SOC ~1 (alloy powder weight 0.8 g; electrode area 7.2 cm^2).

where η $(=E-E_e)$ is the overpotential, i_0 is the exchange current density and the other symbols have their usual meaning. The charge-transfer resistance (R_{ct}) for the electrodes calculated from their impedance data as well as from linear polarization data (Equation 5) are shown in Figure 10(a) as a function of particle size. Although the R_{ct} values obtained from these two methods are slightly different, the trend of their variation with particle size is similar for both methods. The difference in R_{ct} values obtained from the two experimental techniques may be due to the slow potential scan technique in relation to the steady-state technique employed for measuring the linear polarization data.

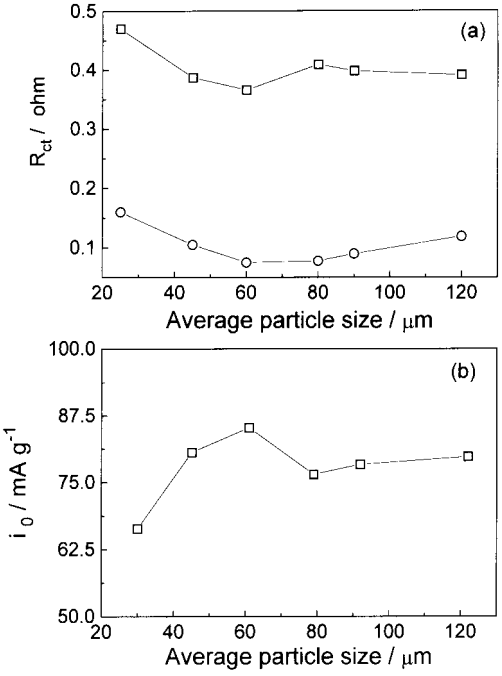

Fig. 10. (a) Charge transfer resistance (R_{ct}) as a function of particle size of the alloy for fully-formed electrodes from impedance spectroscopy (○) and linear-polarization data (□) and (b) the exchange current density (i_0) calculated from linear polarization data as a function of particle size of the alloy particles (alloy powder weight 0.8 g; area 7.2 cm^2).

The lower particle size shows a maximum R_{ct} value and the electrodes with particles of ~60 μm exhibit the least R_{ct} value. As discussed earlier, this increase in R_{ct} value for lower particle size may be due to the presence of a higher oxidized surface on the alloy particles. The exchange current density (i_0) values calculated from the linear polarization method using Equation 5 are also plotted in Figure 10(b) as a function of particle size. The exchange current density is minimum for lower particle size and maximum for electrodes with particle size of ~60 μm. The lower capacity observed for the electrode with smaller particle size (~25 μm) may thus be ascribed to the inactive oxide film, which hinders the charge-transfer process and hence gives a lower exchange current density. It is also evident that the optimum performance observed for the electrodes with average particle size of 60 μm is due to faster electrode kinetics.

3.6. *State-of-charge of the electrodes and electrode kinetics*

The impedance and linear polarization measurements at different state-of-charge (SOC) were also conducted to monitor changes in the electrode kinetics. Impedance plots and linear polarization curves recorded at different SOC values for the electrode with particles of ~60 μm are shown in Figures 11 and 12, respectively. The R_{ct} values obtained from both these methods at different SOC values for electrodes with average particle sizes of 25, 60 and 120 μm are shown in Figure 13. The R_{ct} value gradually increases from the fully-charged state (SOC ~1) of the electrodes to SOC ~0.1; for the fully-discharged electrodes (SOC ~0), it increased to a higher value. This increase may be due to the formation of a passive oxide film on the surface of the alloy particles in the later stage of discharge. A similar trend in variation of R_{ct} as a function of SOC has also been observed for Mm-based alloys [24, 25], and La and La–Zr based alloys [23].

The exchange current density obtained at different SOC values for three different electrodes with particles of 25, 60 and 120 μm, obtained by Equation 5 from the linear polarization data are shown in Figure 14(a) as a function of the SOC values. For electrodes with particle of ~25 μm, the i_0 values decrease almost linearly with SOC of the electrode. But for electrodes with higher particle size (i.e., 60 and 120 μm) the i_0 values initially decrease as the SOC value of the electrode decreases and then exhibit a plateau-like region followed by a steep fall at lower SOC. This variation in i_0 values, particularly, at the lower SOC, may be due to a change in electrode kinetics probably due to the surface oxidation of the alloy particles. Such variation may also be attributed to the change in kinetics of the electrode reaction as the relative amounts of hydride phases change with hydrogen content within the alloy [16]. The i_0 values for the present system are found to be almost double the values observed for La-based AB_5 alloys [18] and much higher than that reported for La [17], Mm and Zr-based alloys [26, 27].

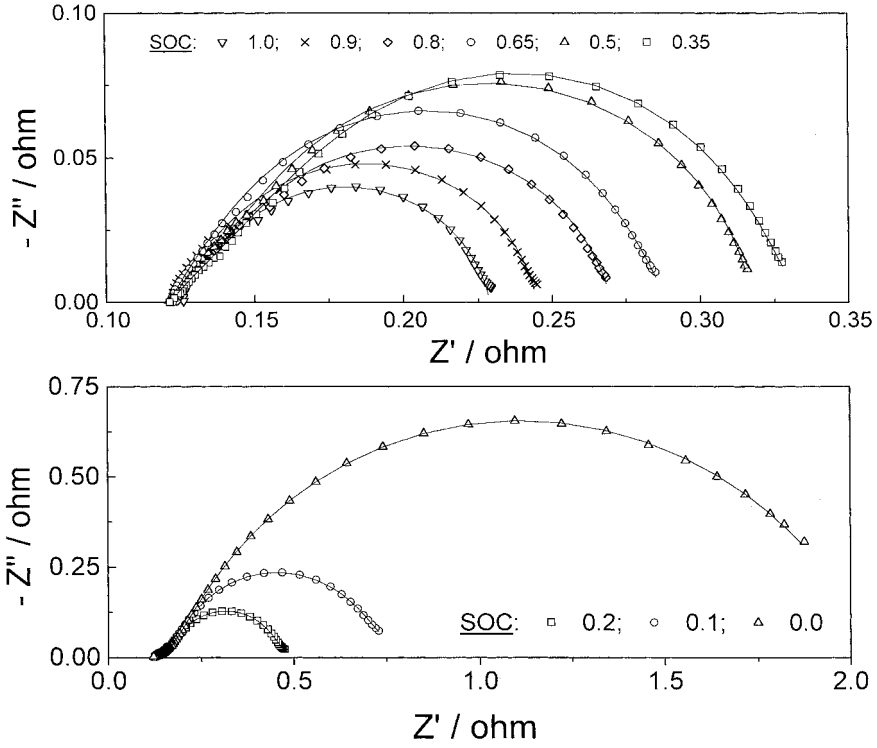

Fig. 11. Impedance plots at different SOC values of a fully-formed electrode of average particle size 60 μm (alloy powder weight 0.8 g; electrode area 7.2 cm^2).

The dependence of equilibrium potential (E_e) on SOC values for electrodes with three different particle sizes are shown in Figure 14(b). As the electrode is discharged from its fully-charged state, the value of E_e decreases at the initial stage of discharge followed by a plateau-like region and again decreases beyond SOC <0.6. The change in E_e values for lower size particles is relatively higher. The E_e of the metal hydride electrodes is proportional to the logarithm of the equilibrium hydrogen pressure of the metal hydride [14, 17]. The E_e against SOC curves can be regarded as isotherms of the hydrogen storage alloy used for electrode fabrication. Therefore, in the present system, the rapid change in E_e values for SOC <0.2 is characteristic of the α-phase or the solid-solution whereas the plateau region is characteristic of the (α + β) phase. The change in slope observed at SOC $\sim$1 is representative of β-phase. The variation in E_e with SOC differs from that reported for AB_5 alloys [14, 18] and, in particular, the plateau region is not clearly distinguishable. Since a plot of the E_e against SOC values is regarded as the isotherm of the system, such a difference is expected [18]. It is noteworthy that while the isotherms of AB_5-alloys show a well-defined plateau region, it is nearly absent for the AB_2-type alloys.

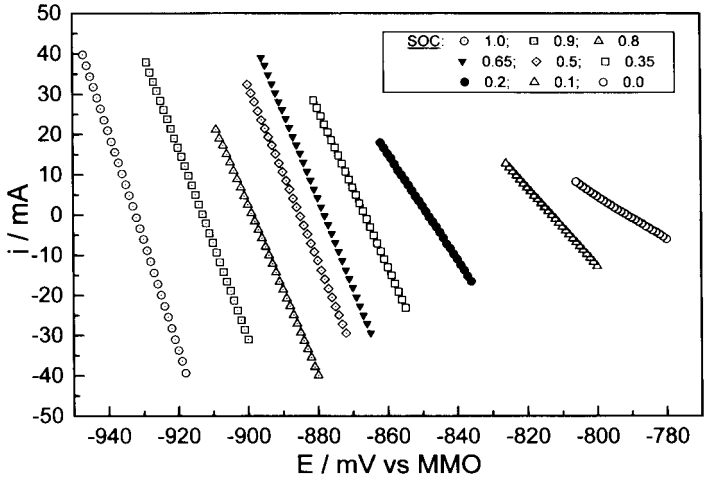

Fig. 12. Linear polarization data obtained at a scan rate of 1 mV s^{-1} for different SOC values of a fully-formed electrode of average particle size 60 μm (alloy powder weight 0.8 g; electrode area 7.2 cm^2).

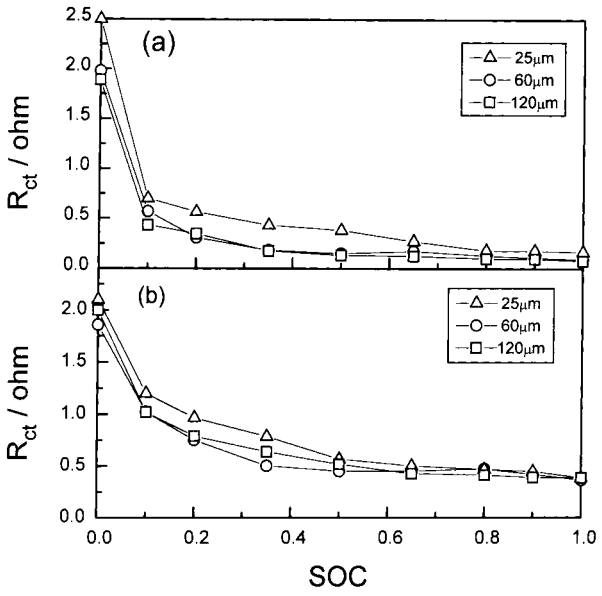

Fig. 13. R_{ct} values obtained from (a) impedance and (b) linear polarization data against SOC values for electrodes of average particle size 25, 60 and 120 μm (alloy powder weight 0.8 g; electrode area 7.2 cm^2).

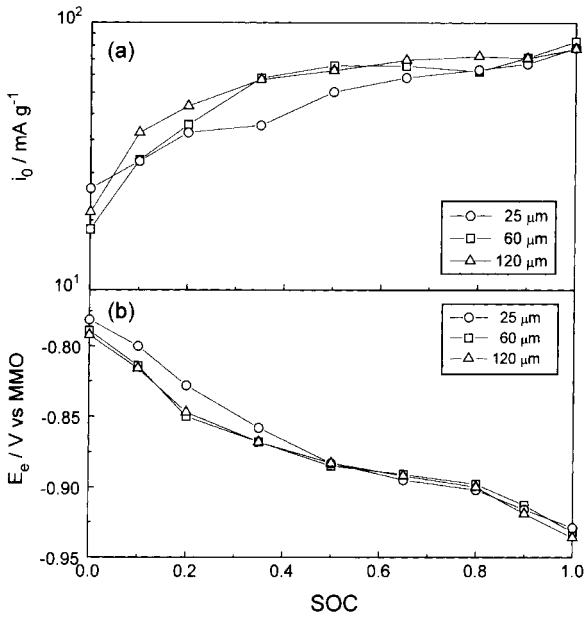

Fig. 14. (a) Exchange current density (i_0), and (b) equilibrium potential (E_e) against SOC of electrodes of average particle size 25, 60 and 120 μm.

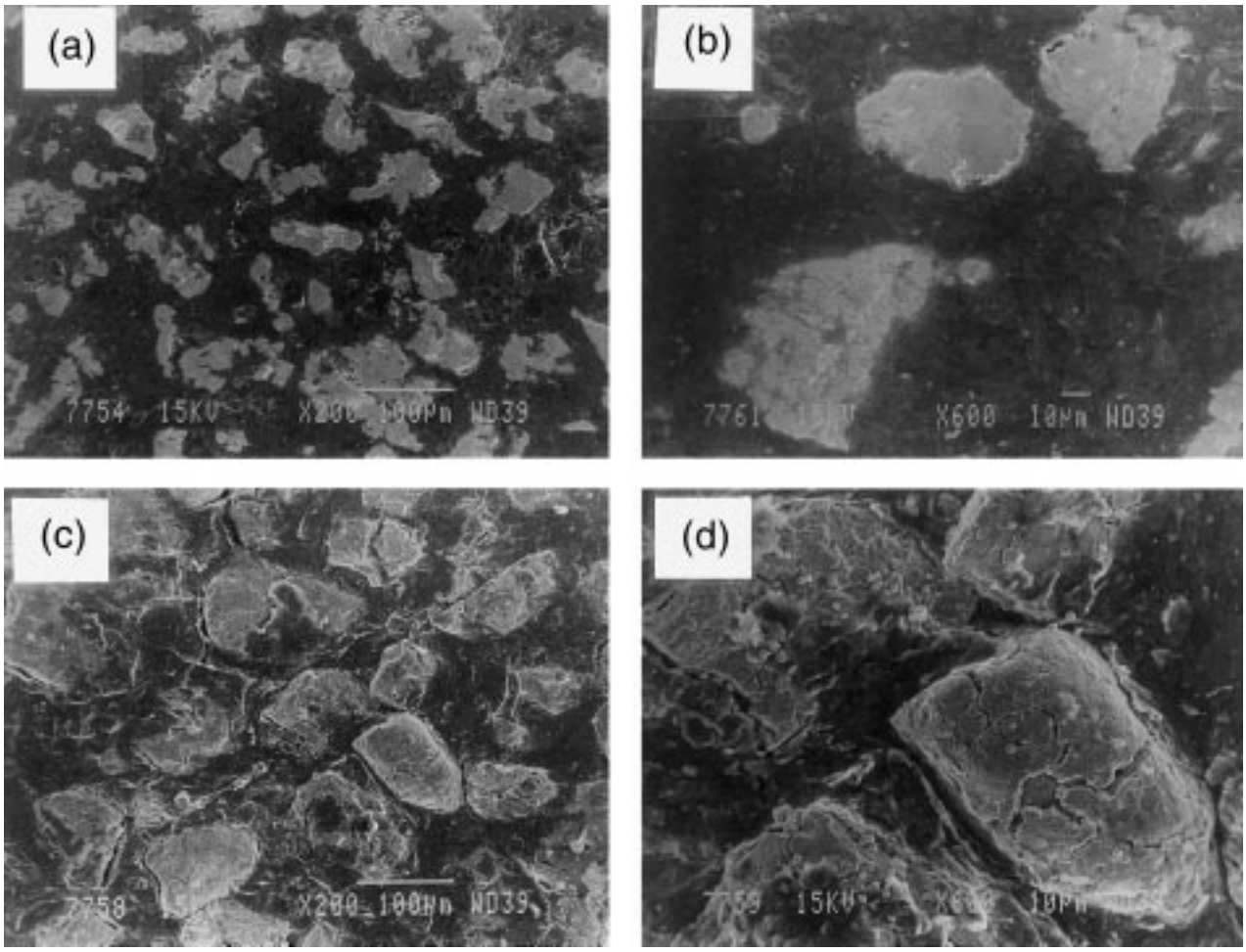

Fig. 15. Electron micrographs for electrodes with average particle size of 60 μm before cycling (a) and (b), and after 50 charge–discharge cycles (c) and (d).

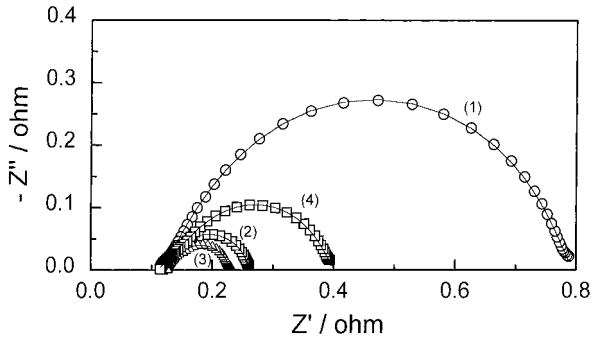

Fig. 16. Impedance plots obtained on fully-charged electrodes (SOC ~1) of 60 μm particles after 2nd (1), 9th (2), 15th (3) and 50th (4) charge–discharge cycles (alloy powder weight 0.8 g; electrode area 7.2 cm^2).

3.7. *Effect of electrode cycling on morphology and electrode kinetics*

A knowledge on the morphology of the metal hydride particles is central to charge–discharge characteristics of the electrodes. The hydrogen storage in the alloy causes a lattice expansion of ~25% with a mechanical strain that leads to the pulverization and passivation of the alloy by surface oxidation. Electron micrographs for electrodes of particle size ~60 μm before and after cycling are shown in Figure 15. The alloy particles do not have surface cracks before charge–discharge cycling of the electrodes (Figure 15(a) and (b)). The electrode structure (Figure 15(a)) also shows compact packing of the alloy particles in the matrix. However, subsequent to 50 charge–discharge cycles, electrode structure and morphology of the alloy (Figure 15(c) and (d)) change significantly and microcracks develop throughout the alloy. There is also a concomitant increase in the volume of the alloy particles during the cycling of the electrodes. Similar observations during cycling of metal hydride electrodes have been reported in the literature [28, 29].

The impedance plots recorded at various cycles for electrodes with alloy particle of ~60 μm clearly show the effect of cycling on electrode kinetics (Figure 16). The charge-transfer resistance is higher for the electrode during initial cycling (curve 1) but decreases during formation and is minimum for the formed electrodes (curve 3). Pulverization of the alloy particles is expected on prolonged cycling of electrodes. The pulverized particles easily undergo oxidation causing an increase in the charge-transfer resistance of the electrodes as observed from the impedance plots recorded after 50 charge–discharge cycles (Figure 16, curve 4).

4. Conclusion

The study suggests an optimum particle size of 60 μm for $Zr_{0.5}Ti_{0.5}V_{0.6}Cr_{0.2}Ni_{1.2}$ alloy to fabricate efficient metal hydride electrodes for nickel/metal hydride cells. These electrodes exhibit faster electrode kinetics and undergo a minimum surface oxidation over their prolonged usage in relation to electrodes of other particle sizes. Electron micrographs obtained on electrodes prior and after their prolonged charge–discharge cycling suggest a significant change in their structure and morphology; this affects the performance of the electrodes. These findings are supported by the a.c. impedance studies on the electrodes.

Acknowledgements

KMS is grateful to the Council of Scientific and Industrial Research, New Delhi for financial support. Our thanks are also due to DMRL-Hyderabad.

References

1. D. Linden, *in* 'Handbook of Batteries', edited by D. Linden (McGraw Hill, New York, 1995), pp. 33.1–33.29.
2. S.R. Ovshinsky, M.A. Fetcenko and J. Ross, *Science* **260** (1993) 176.
3. M.A. Fetcenko, S. Venkatesan and S.R.Ovshinsky, *in* Proceedings of the Electrochemical Society, edited by D.A. Corrigan and S. Srinivasan, **Vol. 92–5**, (The Electrochemical Soc., Pennington, NJ, 1992), pp. 141–167.
4. V. Ganesh Kumar, K.M. Shaju, N. Munichandraiah and and A.K. Shukla, *J. Power Sources* **86** (1998) 106.
5. B. Knosp, C. Jordy, Ph. Blanchard and T.Berlureau, *J. Electrochem. Soc.* **145** (1998) 1478.
6. K.M. Shaju, V. Ganesh Kumar, N. Munichandraiahand and A.K. Shukla, *J. Solid State Electrochem* **3** (1999) 464.
7. C. Lenain, L. Aymard, F. Salver-Disma, J.B. Leriche, Y. Chabre and J.M. Tarascon, *Solid State Ionics* **104** (1997) 237.
8. J. Chen, D.H. Bradhurst, S.X. Dou and H.K. Liu, *J. Alloys Compd.* **265** (1998) 281.
9. H. Inoue, T. Ueda, S. Nohara, N. Fujita and C. Iwakura, *Electrochimi. Acta* **43** (1998) 2215.
10. X. Yang, Y. Lei, C. Wang, G. Zhu, W. Zhang and Q. Wang, *J. Alloys Compd.* **265** (1998) 264.
11. Z. Zhaoliang and S. Dongsheng, *J. Alloys Compd.* **270** (1998) L7.
12. B.V. Ratnakumar, C. Witham, R.C. Bowman Jr., A. Hightower and B. Fultz, *J. Electrochem. Soc.* **143** (1996) 2578.
13. B.S. Haran, B.N. Popov and R.E. White, *J. Power Sources* **75** (1998) 56.
14. N. Kuriyama, T. Sakai, H. Miyamura, I. Uehara, H. Ishikawa and T. Iwasaki, *J. Alloys Compd.* **202** (1993) 183.
15. L.G. Austin, *Trans. Farady Soc.* **60** (1964) 1319.
16. P.H.L. Notten and P. Hokkeling, *J. Electrochem. Soc.* **138** (1991) 1877.
17. G. Zheng, B.N. Popov and R.E. White, *J. Electrochem. Soc.* **143** (1996) 834.
18. B.N. Popov, G. Zheng and R.E. White, *J. Appl. Electrochem.* **26** (1996) 603.
19. B.A. Boukamp, 'Equivalent Circuit, Users Manual' (University of Twente, The Netherlands, 1989).
20. J. Crank, '*The Mathematics of Diffusion*', 2nd edn (Clarendon Press, Oxford, 1975).
21. G. Zheng, B.N. Popov and R.E.White, *J. Electrochem. Soc.* **142** (1995) 2695.
22. C. Iwakura, K. Fukuda, H. Senoh, H. Inoue, M. Matsuoka and Y. Yamamoto, *Electrochim. Acta* **43** (1998) 2041.
23. W. Zhang, M.P. Sridhar Kumar, S. Srinivasan and H.J. Ploehn, *J. Electrochem. Soc.* **142** (1995) 2935.
24. W-K. Hu, D-M. Kim, K-J. Jang and J-Y. Lee, *J. Alloys Compd.* **269** (1998) 254.
25. W-K. Hu, *J. Alloys Compd.* **279** (1998) 295.

26. J. Chen, D.H. Bradhurst, S.X. Dou and H.K. Liu, *J. Alloys Compd.* **265** (1998) 281.
27. D-M. Kim, S-M. Lee, K-J. Jang and J-Y. Lee, *J. Alloys Compd.* **268** (1998) 241.
28. W. Zhang, A. Visintin, S. Srinivasan, A.J. Appleby and H.S. Lim, *J. Power Sources* **75** (1998) 84.
29. Z. Zhou, J. Yan, Y. Li, D. Song and Y. Zhang, *J. Power Sources* **72** (1998) 236.